Bioactive Materials 14 (2022) 402–415

Contents lists available at ScienceDirect

Bioactive Materials

journal homepage: www.keaipublishing.com/en/journals/bioactive-materials

Verteporfin-mediated on/off photoswitching functions synergistically to treat choroidal vascular diseases

Yahan Ju [a,b,1], Xiaochan Dai [a,b,1], Zhimin Tang [a,b,1], Zunzhen Ming [c], Ni Ni [a,b], Dongqing Zhu [a,b], Jing Zhang [a,b], Bo Ma [a,b], Jiajing Wang [a,b], Rui Huang [a,b], Siyu Zhao [a,b], Yan Pang [a,b,**], Ping Gu [a,b,*]

[a] Department of Ophthalmology, Ninth People's Hospital, Shanghai Jiao Tong University School of Medicine, Shanghai, 200011, PR China
[b] Shanghai Key Laboratory of Orbital Diseases and Ocular Oncology, Shanghai, 200011, PR China
[c] Central Laboratory, Shanghai Tenth People's Hospital, Tongji University, Shanghai, 200072, PR China

ARTICLE INFO

Keywords:
Pathological neovascularization
Photodynamic therapy
Bio-responsive release
In situ drug delivery

ABSTRACT

Choroidal vascular diseases, such as age-related macular degeneration, are the leading cause of vision impairment and are characterized by pathological angiogenesis. Verteporfin-mediated photodynamic therapy is a current strategy that selectively occludes choroidal neovasculature. However, the clinically used large-dose systemic administration increases the risk of systemic adverse events, such as phototoxicity to superficial tissues. In this study, we developed an in situ verteporfin delivery system with a photoswitching synergistic function that disassembles in response to intraocular inflammatory enzymes. Under light-on conditions, verteporfin-mediated photodynamic therapy effectively occurs and this leads to vascular occlusion. Under light-off conditions, non-photoactive verteporfin negatively regulates vascular endothelial growth factor-induced angiogenesis as a yes-associated protein inhibitor. Taken together, our system serves as an intraocular verteporfin reservoir to improve the bioavailability of verteporfin by innovatively exploiting its photochemical and biological functions. This work provides a promising strategy with synergistic antiangiogenic effects for the treatment of choroidal vascular diseases.

1. Introduction

The choroid is a highly vascularized network that nourishes photoreceptors and the retinal pigment epithelium (RPE) and removes metabolic wastes from the retina. Choroidal disorders primarily manifest as progressive RPE dysfunction, and choroidal angioarchitecture and functional abnormalities [1], which provoke choroidal vascular diseases (CVDs), such as choroidal neovascularization (CNV) related to age-related macular degeneration (AMD), polypoidal choroidal vasculopathy (PCV) and central serous chorioretinopathy (CSC) [2,3]. Many epidemiological studies have revealed that CVDs affect a wide range of people and that the worldwide prevalence has exponentially increased with each subsequent decade [4,5]. The pathological processes of CVDs are attributed to exudative changes, including increased vascular permeability and neovascularization, resulting in severe damage to visual function or even irreversible blindness [6]. Although CVDs are generally multifactorial and their molecular pathogenesis remains to be elucidated, the abnormal development of the choriocapillaris has been implicated in the elevated production of vascular endothelial growth factor (VEGF) and extensive extracellular matrix (ECM)-related proteins, such as matrix metalloproteases (MMPs), in the inflammatory milieu [7,8].

Clinically, one of the therapeutic strategies to treat CVDs is photodynamic therapy (PDT), which uses a 689 nm laser to activate the injected photosensitizer verteporfin (VP) to generate reactive oxygen species (ROS) and induce vascular endothelial cells (ECs) apoptosis under oxidative stress conditions to reduce leakage and occlude vessels [9,10]. VP-PDT has been widely applied to treat CNV, PCV and other

Peer review under responsibility of KeAi Communications Co., Ltd.
* Corresponding author. 639 Zhizaoju Rd, Shanghai, 200011, China.
** Corresponding author. 639 Zhizaoju Rd, Shanghai, 200011, China.
E-mail addresses: yanpang@shsmu.edu.cn (Y. Pang), guping2009@126.com (P. Gu).
[1] These authors contributed equally to this work: Yahan Ju, Xiaochan Dai and Zhimin Tang.

https://doi.org/10.1016/j.bioactmat.2022.01.028
Received 2 November 2021; Received in revised form 30 December 2021; Accepted 18 January 2022
Available online 1 February 2022

CVDs with encouraging therapeutic effects [11]. However, in order for the drug to reach a sufficient serum concentration when it circulates to the choroidal vascular network, a high injection dose of 6 mg/m^2 of VP (approximately 15 mg) is required in clinical practice [10]. In addition, intravenous administration increases the risk of systemic adverse events, such as photosensitivity reactions, chest pain, and shortness of breath [12,13]. In addition, to avoid damage caused by the photosensitizer to other tissues, especially skin tissue, patients need to be protected from light exposure for at least 48 h after drug injection [14], which makes protection from light exposure inconvenient for patients and leads to poor patient compliance. Moreover, although VP-PDT causes vascular occlusion in pathological neovessels, the superfluous VEGF level in the subretinal space is still a driving force for recurrence, which requires additional combination therapy with *anti*-VEGF drugs [15–17]. Therefore, the development of a new strategy to tackle these problems may be beneficial to patients afflicted with CVDs and encourage better patient compliance.

In addition to its photochemical properties, VP is a potent inhibitor of yes-associated protein (YAP), the pivotal regulator of Hippo-YAP signaling, which has been indicated to be a key signaling pathway in tissue maintenance and organ size regulation [18]. VP can inhibit YAP transcriptional activity in the Hippo pathway, resulting in the regulation of tissue development. Emerging studies have revealed an underlying convergence between VEGF and Hippo-YAP signaling, which has yet to be utilized in clinical applications [19–22]. YAP signaling could act as a hinge to mediate the downstream proangiogenic phenotype. However, whether the combination of the photodynamic and non-photodynamic functions of VP plays a role in hindering the formation of pathological neovascularization remains to be elucidated.

In situ gelling systems for posterior ocular drug delivery have the capacity to improve the bioavailability of ophthalmic pharmaceutical formulations [23–25]. In the present study, we report a light-on/light-off drug delivery system using the Food and Drug Administration (FDA)-approved amphiphilic agent triglycerol monostearate (TGMS) to encapsulate VP. The in situ gelling system is stimuli-responsive to the increased expression of MMP-2 and MMP-9 in the vitreous cavity of CVDs [8,26–28]. Notably, our drug delivery system was designed to offer the following benefits: 1) Under light-on conditions, this system could utilize a low dose of VP to achieve comparable therapeutic effects and simultaneously avoid systemic photosensitive reactions, which achieved the symptomatic efficacy of photoactivated VP. 2) Under light-off conditions, this system could realize the effects of non-photoactivated VP as a YAP inhibitor on VEGFR2 signaling, thus implementing an etiological therapy (Graphical abstract). Importantly, our system benefits the most from the physicochemical and biological functions of VP under light-on and light-off conditions to greatly augment the synergistic efficacy of anti-angiogenic treatment, which may provide new insights for the treatment of CVDs.

2. Materials and methods

2.1. Preparation of the hydrogel and drug encapsulation

To prepare VP-loaded TGMS hydrogels (VP-TGMS, 10%, w/v), 1 g of TGMS (Shanghai Yuanye Bio-Technology, China) was weighed and added to 10 mL of DMSO water mixture (8 mL of sterile water and 2 mL of DMSO) in a scintillation vial with a stir bar. The vial was suspended in a beaker filled with water and heated to 60–80 °C using a magnetic stirrer. After the TGMS dissolved and the solution became homogeneous, 3 mg of VP (MedChemExpress, USA) was added to the vial (0.3 mg/mL). After cooling to room temperature for approximately 30 min, VP-TGMS became gelatinous, and no gravitational flow was observed upon inversion of the vial. These hydrogels were easily injectable using 30-G needles or micropipettes.

2.2. Drug loading experiment

According to published method [29], VP solutions with different concentrations of VP were prepared to obtain a standard curve in DMSO by measuring the fluorescence intensity at an excitation wavelength of 420 nm and an emission wavelength of 680 nm using a Synergy H1 microplate reader (BioTek, USA). VP-TGMS gels with different feeding concentrations of VP were prepared and dissolved in PBS. Free VP was separated from the VP-TGMS by centrifugation (12,000 rpm, 20 min). The supernatant with unencapsulated VP was collected, frozen, lyophilized, and resuspended in DMSO to solubilize the unencapsulated VP in the release solution. The mass of VP was measured again using a microplate reader. The amount of free VP was then back-calculated from the standard curve. The loading efficiency (LE) and encapsulation efficiency (EE) of VP were calculated using the following equations:

LE (%) = (weight of loaded VP in VP-TGMS hydrogels [mg])/(total weight of hydrogels [g]) × 100%

EE (%) = (weight of loaded VP in VP-TGMS hydrogels [mg])/(weight of feeding VP [mg]) × 100%

2.3. Characterization of VP-TGMS

Scanning electron microscopy (SEM) measurements were performed using an FEI nanoSEM NOVA230 microscope. VP-TGMS gels were generated by lyophilization, and the morphology of the samples was characterized by SEM at an operating voltage of 5 kV. The rheological properties of the injectable VP-TGMS hydrogels were explored using a Thermo Fisher Scientific rheometer (HAAKE MARS III) with a 20-mm parallel plate. The frequency for the strain sweep and time sweep measurements was set to 10.0 rad/s. The pH values were detected in the micellar solution before VP-TGMS became a gel state using a handheld pH meter (OHAUS ST-300). The osmolarity of the VP-TGMS gels was tested with a colloid osmometer (OSMOMAT 050). The recording system was calibrated prior to each experiment. Swelling studies were carried out to assess the hydration capacity of the VP-TGMS gels at 37 °C. The initial mass of the VP-TGMS hydrogel (W_0) was recorded. Subsequently, the VP-TGMS hydrogels were immersed in PBS. The mass of swollen hydrogels in equilibrium at each time point (W_t) was then measured. Three samples were used at each time point in the study. The swelling ratio was calculated using the following equation: swelling ratio = ($W_t - W_0$)/W_0.

2.4. Detection of MMP-2/9 levels in vitreous samples

Vitreous samples from patients were obtained from the Ninth People's Hospital, Shanghai Jiao Tong University School of Medicine following approval by the institutional research ethics board (No. SH9H-2021-T96-2). Vitreous humor samples were obtained from PCV patients during vitrectomy, and control samples were obtained from the enucleated eyes of patients without CVDs. The vitreous humor specimens were centrifuged (5000 rpm, 2 min), and the supernatants were immediately frozen at −80 °C until detection. Vitreous humor levels of MMP-2/9 were detected using a Human MMP-2 ELISA Kit (RayBiotech, USA) and Human MMP-9 ELISA Kit (RayBiotech, USA), respectively, according to the manufacturer's instructions.

2.5. Enzyme-responsive drug release

VP-TGMS samples (VP, 0.3 mg/mL, 200 μL) were suspended in PBS (10 mL, pH = 7.4) in a 15-mL centrifuge tube with or without recombinant human MMP-2 (100 ng/mL, R&D Systems, USA), recombinant human MMP-9 (15 ng/mL, R&D Systems, USA) or lipase (500 U/mL or 1000 U/mL, *Aspergillus oryzae*, Sigma–Aldrich, USA). Under certain

conditions, the MMP-2/9 inhibitor ilomastat (10 nM, MedChemExpress, USA) was added together with MMP-2/9. The tubes were incubated at 37 °C in a humidified atmosphere. Fresh enzyme or inhibitor was added to the PBS solution at the determined time points. An aliquot (100 μL) was removed from the release solution, and the same volume of fresh PBS was replenished to ensure a constant volume. Collected aliquots were frozen, lyophilized, and resuspended in DMSO followed by fluorescence intensity detection. The mass of the VP released was back-calculated using standard curve.

2.6. Cell cultures

Human umbilical vein endothelial cells (HUVECs) were purchased from ScienCell (USA) and were cultured in endothelial cell medium (ScienCell, USA) containing 5% fetal bovine serum (FBS, ScienCell, USA), 1% endothelial cell growth supplement (ECGS, ScienCell, USA) and 1% penicillin/streptomycin (ScienCell, USA). For the *in vitro* assessment of angiogenesis, HUVECs were incubated with or without recombinant human $VEGF_{165}$ (PeproTech, USA) for the indicated time in medium without ECGS. ARPE-19 cells, a human retinal pigment epithelium cell line, were cultured in Dulbecco's modified Eagle's medium (DMEM, Gibco, USA) supplemented with 10% FBS (Gibco, USA) and 1% penicillin/streptomycin (Gibco, USA). 661W cells (a mouse photoreceptor cell line) were cultured in F–12K nutrient mixture medium (Gibco, USA) containing 10% FBS and 1% penicillin/streptomycin. Human Müller cells (MIO-M1) were cultured in DMEM/F12 medium containing 10% FBS and 1% penicillin/streptomycin. All cells were cultured at 37 °C under 5% CO_2 in a humidified atmosphere.

2.7. Cell viability detection

ARPE-19 cells, 661W cells, and Müller cells were seeded in 24-well plates (4×10^4/well). Then, 100 μL of Blank-TGMS or VP-TGMS hydrogel was added to incubate the cells in the culture inserts for 48 h. Cells cultured in normal medium were used as the control. After treatment, the cells were digested and centrifuged for seeding in 96-well plates with an equal volume of cell suspension. Then, the three types of cells with different treatments were incubated with Cell Counting Kit-8 (CCK-8) for 4 h. After 4 h of incubation, the optical density was measured using a microplate reader at a wavelength of 450 nm. Cell viability was expressed as a percentage normalized to the value of the control group.

2.8. Western blotting analysis

Total proteins from the treated cells were harvested in RIPA lysis buffer (Thermo Scientific, USA) with a 1% protease and phosphatase inhibitor cocktail and then sonicated. Protein concentration was determined using a BCA protein assay kit (Thermo Scientific, USA). Equal amounts of lysate (50 μg) were separated on SDS–PAGE gels (Bio–Rad, USA), transferred to PVDF membranes (Millipore, USA) and then blocked in 5% BSA for 1 h. The membranes were then incubated with primary antibodies (*anti*-IL-6 [1:1000, Absin, China], *anti*-MCP-1 [1:1000, Proteintech, China], *anti*-β-actin [1:2000, Cell Signaling Technology, USA], *anti*-MMP-2 [1:1000, Santa Cruz Biotechnology, USA], *anti*-MMP-9 [1:1000, Cell Signaling Technology, USA], *anti*-phosph-VEGFR2 [1:1000, Cell Signaling Technology, USA], *anti*-VEGFR2 [1:1000, Cell Signaling Technology, USA], *anti*-phosph-YAP [1:1000, Cell Signaling Technology, USA] and anti-YAP [1:1000, Cell Signaling Technology, USA]) at 4 °C overnight and then probed with horseradish peroxidase (HRP)-conjugated secondary antibodies. Protein signaling was visualized using Tanon-5200 image scanning system (Tanon, China).

2.9. In vitro detection of singlet oxygen production

The PDT efficiency of the VP-TGMS hydrogels was evaluated by detecting the generation of singlet oxygen ($^1O_2$) *in vitro* with a singlet oxygen detection kit (BBoxiProbe O22, BestBio, China). HUVECs were seeded in 24-well plates (500 μL) cocultured with 100 μL Blank-TGMS, VP-TGMS in the culture inserts for 24 h after culturing to 100% confluence. Then, cells from the VP group served as a positive control and were cultured in medium supplemented with 4 μM of free VP (dissolved in DMSO and diluted with medium). The cells in the VP-TGMS and VP groups were irradiated with a 689 nm laser (600 mW/cm^2) for 1 min. Subsequently, the cells were immediately incubated with singlet oxygen fluorescent probes in serum-free culture medium for 4 h according to the manufacturer's protocol. Then, the cells were washed with PBS for a few seconds, and images were then taken using fluorescence microscopy with an excitation wavelength of 488 nm. The detected green fluorescence was due to the oxidized substances accumulated in the cells within 4 h.

2.10. Live/dead staining

HUVECs (500 μL) seeded in 24-well plates in the Blank-TGMS and VP-TGMS groups were pretreated with Blank-TGMS (100 μL) or VP-TGMS (100 μL) for 24 h after culturing to 100% confluence. After this procedure, free VP (4 μM) was added to the medium to incubate the cells in the VP group. Then, some cells from the VP-TGMS and VP groups were irradiated with a 689 nm laser (600 mW/cm^2) for 1 min. Cells from all groups were stained with calcein AM reagent (live cells) and PI reagent (dead cells) using a live/dead staining kit (Invitrogen, USA) for fluorescence microscopy (Nikon) imaging.

2.11. Animals

All *in vivo* experiments were performed in accordance with Association for Research in Vision and Ophthalmology (ARVO) statements, and the procedures were approved by the Institutional Animal Care Committee of the Ninth People's Hospital, Shanghai Jiao Tong University School of Medicine (no. HKDL2018507). In the present study, male C57BL/6J mice (6–8 weeks old, 20–25 g) and male BALB/c nude mice (6 weeks old, 20–24 g) were purchased from Sino-British SIPPR/BK Lab Animal Ltd. (Shanghai, China). All mice were housed in a specific pathogen-free (SPF) environment. Mice used in this study were anesthetized with anesthetic solutions prepared with tiletamine (10 mg/kg), zolazepam (10 mg/kg) (Zoletil 50®, England) and dexmedetomidine hydrochloride (0.05 mg/kg) (Dexdomitor®, USA).

2.12. Laser-induced CNV

The laser-induced CNV mouse model was generated according to a previously established method [30]. Male C57BL/6J mice (6–8 weeks old, 20–25 g) were used to generate the CNV model. After deep anesthesia and dilation of the pupils with tropicamide and phenylephrine eye drops (0.5%, Santen Pharmaceutical, Japan), a lab-made corneal contact lens was used to visualize the retina with a slit lamp. Laser photocoagulation (532 nm, 450 mW, 50 ms and 50 μm spot size) was delivered to four positions around the optic disc for each eye. The appearance of a bubble at the site of laser injury indicated disruption of Bruch's membrane and confirmed the successful establishment of laser-induced CNV.

2.13. Administration

For intravitreal injection, mice were anesthetized first, their pupils were diffused, and the ocular surface was topically anesthetized with oxybucaine hydrochloride eye drops. We then made an incision at 1 mm posterior to the limbus under a stereomicroscope by a 0.3-mm-diameter

needle. After pulling out the needle, a flat needle was inserted along the incision with a microsyringe, followed by slow injection of 2 μL of saline, Blank TGMS and VP-TGMS (0.3 mg/mL). For the control group, mice were received intravenous injection of VP saline solution (100 μL, 6 mg/m^2) with DMSO as a co-solvent for VP via the tail vein. The dose of VP for intravenous injection is based on the optimal parameter for the treatment of CNV on animal models and clinic [9,31,32]. In the PDT treatment group, laser light at a wavelength of 689 nm and a spot size of 300 μm induced selective activation of VP was chosen in the target area though a slit lamp adaptor (Quantel Medical, USA). A laser irradiance of 600 mW/cm^2 was delivered for 83 s (the clinically used length of time) to achieve 50 J/cm^2 light energy. In the non-PDT treatment group, mice were placed under a standard lighting regimen of 15–20 lx.

2.14. Histological staining

After the mice were sacrificed, their eyeballs were carefully removed and fixed in FAS eyeball fixative solution (Servicebio). The eyes were then prepared into paraffin sections (5 μm thickness). The slices were then dewaxed in xylene and rehydrated. For hematoxylin-eosin (H&E) staining, the slices were stained with H&E at 37 °C for 1 h. For the TUNEL assay, TUNEL detection solution mixture (fluorescent labeling solution and TdT enzyme with 50:1 ratio) was added to the samples which were then incubated at 37 °C for 2 h. The cell nuclei were labeled with DAPI staining solution. Images were acquired by fluorescence microscopy (Nikon) focused on the superior hemisphere section of the retina 0.2 mm from the optic nerve head.

2.15. Intraocular pressure (IOP) measurement

To assess whether the hydrogel affected the IOP of mice, IOP measurements were conducted after drug administration for 1 day. Mice were prepared for IOP measurement using a TonoLab rebound tonometer (Icare, Finland) without anesthesia. All measurements were performed by the same researcher.

2.16. Electroretinogram (ERG)

ERG was performed as described previously [33]. To evaluate whether the hydrogel affected the visual function of mice, ERG was recorded in the mice after administration for 7 days using an Espion E3 system (Diagnosys, USA) under dim red light. The mice were deeply anesthetized and their pupils were dilated after dark adaptation for 24 h. The mice were then placed on a heating pad throughout the test to avoid detection errors caused by hypothermia. The foreheads and tails of the mice were linked to the reference and ground electrodes, respectively. A pair of gold loop electrodes was attached to the cornea. The retinal response to a single stimulus flash (10 cd s m^{-2}) was recorded under dark-adapted conditions (scotopic ERGs).

2.17. In vivo degradation of the hydrogels

In vivo degradation of the TGMS hydrogel was determined using a subcutaneous implantation model with male BALB/c nude mice (6 weeks old, 20–24 g). The mice were deeply anesthetized. After their skin surface was disinfected with iodophor, 100 μL of the TGMS hydrogel was injected subcutaneously. The longest and shortest diameters of the phyma were measured with calipers at predetermined times, and the volume of residual subcutaneous hydrogel was calculated using the following equation:

$V\ (mm^3) = 1/2 \times L \times W^2$ (L = longest diameter of the phyma, W = shortest diameter of the phyma)

2.18. Fluorescein angiography (FA)

FA was performed to observe fluorescence leakage after laser photocoagulation. After anesthesia and dilation of the pupils, the mice were intraperitoneally injected with 0.05 mL of 10% fluorescein sodium solution (Alcon, China). FA and IR photographs of the posterior segments were acquired sequentially using Heidelberg Spectralis HRA system (Heidelberg Engineering Inc., Germany) at 3 min post-injection. The level of vascular leakage was determined by measuring the fluorescence pixel intensity using the ImageJ software.

2.19. Fluorescence imaging of RPE-choroid flat-mounts

After the mice were sacrificed, the eyeballs were carefully enucleated and fixed in FAS eyeball fixative solution (Servicebio) for 3 h at room temperature. The RPE-choroid flat mounts were carefully removed from the eyecups and made into four incisions. After being blocked with 5% goat serum in PBST (0.3% Triton X-100 in PBS) for 1 h, the flat mounts were stained with FITC-GSL I-Isolectin B4 (IB4) (1:200, Vector, France) at 4 °C overnight. After the flat mounts were washed with blocking solution, images were acquired with a fluorescence microscope (Nikon). The area of CNV-related fluorescence was determined using ImageJ software.

2.20. Transwell assay

A 200 μL suspension of 5 × 10^4 HUVECs was seeded in the upper chambers of 24-well plates (8.0-μm pores, Corning, USA), while 800 μL of medium with different treatments (①DMSO (in an amount equal to that of the VP group), ②VEGF (200 ng/mL)+DMSO, ③VEGF (200 ng/mL)+ VP (4 μM), ④VEGF (200 ng/mL) + Blank-TGMS (100 μL), ⑤VEGF (200 ng/mL) + VP-TGMS (0.3 mg/mL, 100 μL), ⑥VEGF (200 ng/mL) + VP-TGMS (0.3 mg/mL, 100 μL)+lipase (500 U/mL) was added into the lower chambers. After treatment for 15 h, the cells were fixed with 4% paraformaldehyde for 20 min, and cells from the upper surface of the inserts were carefully wiped with a cotton swab. The inserts were then stained with crystal violet dye (1%) for 30 min. The cells that migrated from the lower surface were imaged under a microscope. ImageJ software was used to count the migrated cells.

2.21. Scratch assay

HUVECs were seeded in 6-well plates. When cell confluence reached 100%, a homogeneous cell-free area was created using a 200 μL pipette tip on the confluent cell monolayer. Scratch images were captured at the beginning of the experiment (0 h). Then, cells were cultured with fresh low-serum medium (2 mL) supplemented with 1% FBS with or without 200 ng/mL VEGF. In the VEGF-stimulated group, HUVECs were cotreated with DMSO (in an amount equal to that of the VP group), VP (4 μM), Blank-TGMS (200 μL), VP-TGMS (0.3 mg/mL, 200 μL) or VP-TGMS (0.3 mg/mL, 200 μL) +lipase (500 U/mL) in the culture inserts. Cells were cultured for an additional 24 h, and after that, scratch images were recorded at the same location. Cell migration was assessed by measuring the percentage of wound closure using ImageJ software.

2.22. Tube formation assay

Matrigel (150 μL, Corning, USA) was precoated on a 24-well plate and polymerized for 1 h at 37 °C. After that, HUVECs (4 × 10^4/well, 1 mL) were seeded on the polymerized Matrigel in endothelial cell medium without ECGS and with or without VEGF (200 ng/mL). In the VEGF-stimulated group, HUVECs were cotreated with DMSO (in an amount equal to that of the VP group), VP (4 μM), Blank-TGMS (100 μL), VP-TGMS (0.3 mg/mL, 100 μL) or VP-TGMS (0.3 mg/mL, 100 μL) +lipase (500 U/mL) in the culture inserts. After 8 h of treatment, images of tube formation were captured. Capillary-like tube networks were

observed, and the number of tubes, branches and nodes were counted. Images were inverted to observe tube formation more clearly.

2.23. RNA extraction, RNA sequencing, and qPCR

RNA extraction: After serum starvation for 12 h, HUVECs were divided into two groups: VEGF and VEGF + VP. Cells from the VEGF + VP group were pretreated with VP (4 μM) for 2 h, and then all cells were treated with VEGF (200 ng/mL) for another 24 h. Subsequently, total RNA from HUVECs was prepared using TRIzol reagent, and an mRNA library was thus constructed.

RNA sequencing: RNA sequencing was carried out by BGI (Beijing Genomic Institute, ShenZhen, China). SOAPnuke software (v1.5.2) was used to filter the data for RNA sequencing, and then these data were mapped to the reference genome using HISAT2 software (v2.0.4). The clean reads were aligned to the gene set by Bowtie2 (v2.2.5). The expression levels of the genes were then measured with RSEM software (v1.2.12). A heatmap of the top 40 differentially expressed genes was constructed according to the gene expression with fragment per kilobase of transcript per million (FPKM). Reactome (https://www.reactome.org/) enrichment analysis of differentially expressed genes was performed, and the significant levels of terms and pathways were corrected by the Q value. The results of RNA sequencing have been submitted to the GEO database (accession number: GSE181880).

qPCR: Reverse transcription of total RNA from HUVECs was performed using PrimeScript RT master mix (Takara, Japan). Real-time qPCR to measure mRNA expression levels was performed with SYBR Green PCR Mix (Applied Biosystems, USA) as our previous study reported [34]. GAPDH was utilized as an internal control to normalize mRNA expression, and mRNA expression is presented as the relative fold change compared to the control group. The sequences of all primers used are listed in Table S1 (Supplementary Materials).

2.24. Statistical analysis

All statistical data obtained from independent experiments are expressed as the mean ± standard deviation (SD) as obtained from GraphPad Prism 7.0 throughout this study. Values of $^{*}P < 0.05$ and $^{**}P < 0.01$ were considered statistically significant.

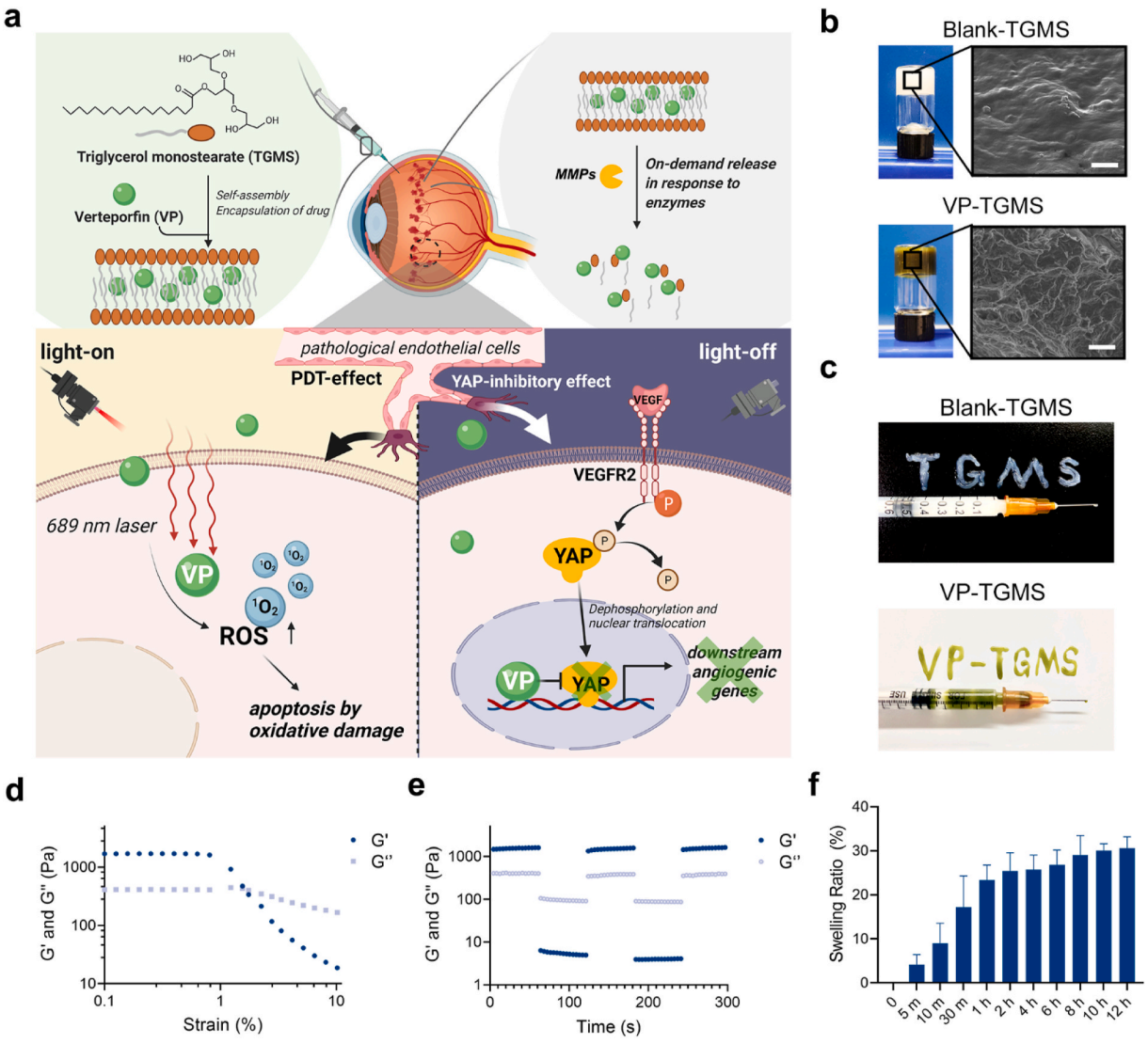

Fig. 1. Preparation and characterization of the VP-loaded TGMS hydrogel. **(a)** Schematic illustration of VP-TGMS hydrogel self-assembly and enzyme-responsive VP release for treating CVDs. **(b)** Scanning electron microscopy (SEM) of the Blank-TGMS and VP-TGMS hydrogels. Scale bars: 10 μm. **(c)** Photographs showing the injectable behavior of the Blank-TGMS and VP-TGMS hydrogels. **(d)** Strain-dependent oscillatory measurements of the VP-TGMS hydrogel. **(e)** Step–strain measurements of the VP-TGMS hydrogel by rheology analysis. **(f)** Swelling ratio of the VP-TGMS hydrogel in PBS at determined time points.

3. Results and discussion

3.1. Synthesis and characterization of the VP-TGMS hydrogel

The intraocular space has a delicate anatomical and biological nature, so in situ drug delivery carriers need to have excellent biocompatibility and characteristics that allow adaptation to CVDs. TGMS is an FDA-approved, generally recognized as a safe (GRAS) agent with certain properties, including amphipathy, self-assembly and enzymatic hydrolyzation. It has a Krafft temperature of 55–60 °C and is composed of a hydrophilic polyglycerol head group and a hydrophobic stearate tail. After being heated to 60 °C, TGMS can dissolve in a DMSO/water mixture, and self-assemble into a hydrogel to encapsulate VP in the hydrophobic core of the formed micelles after cooling. There is an ester bond in the hydrophobic tail of TGMS that can be cleaved by enzymes such as esterases and MMPs under inflammatory conditions, leading to the release of the encapsulated VP (Fig. 1a). To take advantage of the good gelling properties of TGMS, we encapsulated VP in 10% (w/v) TGMS gels. We further analyzed the encapsulation efficiency (EE) and loading efficiency (LE) of VP in the VP-TGMS gels at different feeding concentrations to evaluate the drug-loading capacity. The results showed that the EE% and LE% of VP-TGMS hydrogel were 92.15 ± 0.33% and 22.89 ± 1.32%, respectively, when the feed concentration reached 0.3 mg/mL (Fig. S1a). However, as the concentration of the feeding drug increased to 0.5 mg/mL, the EE% decreased significantly (<65%), but there was no corresponding obvious increase in LE%, indicating that a higher VP feeding dose might affect the self-assembly of VP-TGMS gel. Therefore, we chose 0.3 mg/mL VP for subsequent *in vitro* and *in vivo* studies. Scanning electron microscopy (SEM) images show the ultrastructural morphology of the Blank-TGMS hydrogel and VP-TGMS hydrogel (Fig. 1b). Compared to the Blank-TGMS hydrogel, VP-TGMS hydrogels present a porous structure. The possible reason might be that hydrophobic interaction of polymethylene hydrocarbon chain encapsulating the hydrophobic VP in the core of micelles changed the structure of hydrogels. Additionally, the Blank-TGMS and VP-TGMS hydrogels can be easily injected using 1 mL syringes using 30-G needles (Fig. 1c). To explore the mechanical properties of the VP-TGMS hydrogels, strain-dependent oscillatory measurements were performed with a stress-controlled rheometer. As shown in Fig. 1d, the critical strain value at which the gel network was disrupted and transformed to a liquid state was observed at 1.5%, further indicating the excellent shear-thinning properties of the hydrogel. Step–strain measurements were performed to examine the recovery abilities of the hydrogel mechanical properties. As illustrated in Fig. 1e, when the gel was subjected to high-magnitude strain (100%), G' (elastic modulus) dropped sharply from ~1600 Pa to ~5 Pa, which was less than the G'' (loss modulus), suggesting network disruption. The mechanical properties of the hydrogel recovered completely within a few seconds when the high strain was discontinued and a low magnitude strain ($\gamma = 0.1\%$) was applied at this stage. Therefore, the mechanical properties of the VP-TGMS gel could recover after several breaking and reforming cycles, further indicating the robust reversibility and injectability of this material. To further explore whether VP-TGMS is suitable as an intraocular drug delivery vehicle, the pH and osmolality of VP-TGMS were determined in this study. The pH value of the VP-TGMS micellar solution was measured at 7.88 ± 0.02, which is within the tolerant pH range (4–8) of human eyes [35] (Fig. S1b). Osmolality testing of the VP-TGMS hydrogel resulted in a value of 281 ± 3.7 mOsm/kg (Fig. S1b), which is close to that of human vitreous humor (289.5 ± 6.9 mOsm/kg tested from 24 individual samples [36]). Additionally, the swelling ability was also detected for VP-TGMS gel. As shown in Fig. 1f, the swelling ratio of the VP-TGMS hydrogel increased and gradually stabilized within 12 h. More specifically, the swelling ratio of VP-TGMS gel in PBS increased from 23.4% to 30.6% between 1 h and 12 h. Both the suitable colloid osmolarity and the relatively low swelling ratio of VP-TGMS could avoid surrounding tissue damage caused by liquid penetration and excessive swelling, which makes it more suitable for intravitreal injection.

3.2. VP release from the VP-TGMS hydrogel in response to enzymes

Disassembly and remodeling of the ECM are two prerequisites for neovascular invasion. The expression and secretion of gelatinases (MMP-2 and MMP-9) from the MMP family can be redeployed in response to ECM regulation [37]. It has been reported that intraocular MMP-2 and MMP-9 remain at low expression levels under normal conditions, while their expression increases under pathological conditions, such as during neovascular disease [38]. In addition, considering that TGMS gels have an enzyme-responsive capacity, we next investigated the expression levels of MMP-2 and MMP-9 in the vitreous humor of eyes with CVDs. The ELISA results demonstrated that MMP-2 and MMP-9 levels were significantly upregulated in the vitreous humor samples of PCV patients compared to control samples ($p = 0.0041$ and $p = 0.0025$, respectively) (Fig. 2a and b). Additionally, we observed elevated protein expression levels of MMP-2/9 in the retina-RPE-choroid complexes from laser-induced CNV mouse models ($p = 0.0155$ and $p = 0.0063$, respectively) (Fig. S2), which is consistent with the latest work [39]. Together, these results suggest that intraocular pathological angiogenesis can induce MMP-2/9 stimulation.

Next, we evaluated the enzyme-responsive capacities of the VP-TGMS hydrogel to disassemble and release the encapsulated VP *in vitro*. VP-TGMS gels were incubated in PBS with or without lipase (500 U/mL or 1000 U/mL), MMP-2 (100 ng/mL), or MMP-9 (15 ng/mL). The concentrations of MMP-2 and MMP-9 were chosen based on the value detected in vitreous samples (Fig. 2a and b). As shown in Fig. 2c, repeated pulses of lipase led to the significantly higher accumulative release of VP ($p < 0.0001$), while VP-TGMS in PBS exhibited a stable state with no obvious hydrolysis. The on-demand release of VP was further observed with the multiple additions of MMP-2 (100 ng/mL) or MMP-9 (15 ng/mL) at the determined time points. Compared with the control group in PBS, the cumulative VP release increased by 32.02 ± 2.29% ($p < 0.0001$) and 14.62 ± 1.40% ($p = 0.0023$) on day 28, respectively (Fig. 2d and e). Notably, with the pre-addition of the MMP-2/9 inhibitor, the release of the encapsulated VP in solutions containing MMP-2 or MMP-9 was significantly suppressed. Therefore, our VP-loaded MMP-responsive hydrogels enabled stimuli-responsive delivery and controlled release of the photosensitizer.

3.3. In vitro biocompatibility and photodynamic effects of VP-TGMS

We first evaluated the *in vitro* biocompatibility of the VP-TGMS hydrogel with three types of retinal cells: ARPE-19 cells (a human retinal pigment epithelium cell line), 661W cells (a mouse photoreceptor cell line) and human retinal Müller cells. Cells were incubated under basal conditions or in medium with Blank-TGMS or VP-TGMS (protected from light) added to the culture inserts for 48 h. Cell viability was then assessed, and no difference in cell viability was found among the three types of cells after the different treatments, suggesting good biocompatibility of the TGMS hydrogels with *in vitro* retinal cells (Fig. 3a). Inflammation is strongly associated with CVDs and promotes progression of angiogenesis [40]. To assess whether TGMS hydrogels could cause an inflammatory response in treated cells, the protein expression levels of the inflammatory cytokines IL-6 and MCP-1 (two main factors triggering ocular inflammatory diseases [41,42]) in the treated cells were detected by western blotting. No obvious increase in the expression of IL-6 or MCP-1 was observed in the cells incubated with hydrogels (Fig. 3b), further indicating the biosafety of the TGMS gels.

ECs regulate the establishment of neovascular disorders and are the clinical target of PDT. As a photosensitizer, VP can generate toxic singlet oxygen ($^1O_2$) upon irradiation with laser in the target area, which leads to ECs apoptosis [10]. Subsequently, we investigated the photodynamic effects of the VP-TGMS hydrogel on HUVECs following laser activation. According to the phototoxic evaluation of different concentrations of

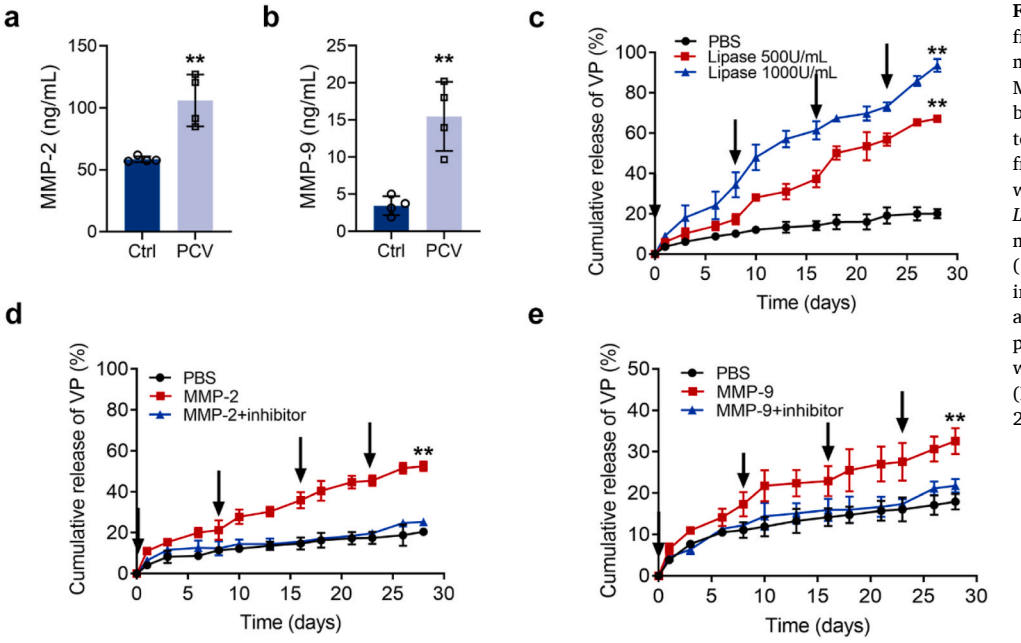

Fig. 2. Enzyme-responsive release of VP from VP-TGMS hydrogels *in vitro*. **(a, b)** The mean concentrations of (a) MMP-2 and (b) MMP-9 in the vitreous samples determined by ELISA (n = 4). **P < 0.01 by Student's *t*-test. **(c–e)** In vitro release kinetics of VP from VP-TGMS hydrogels in PBS at 37 °C with or without (c) lipase (*Thermomyces Lanuginosus* lipase, 500 U/mL or 1000 U/mL), (d) MMP-2 (100 ng/mL), (e) MMP-9 (15 ng/mL). VP-TGMS hydrogels were incubated with lipase, MMP-2, MMP-9 and an MMP-2/9 inhibitor at the indicated time points (arrows) (n = 3). **P < 0.01 by one-way ANOVA followed by LSD post hoc test (PBS versus enzyme-treated groups on day 28).

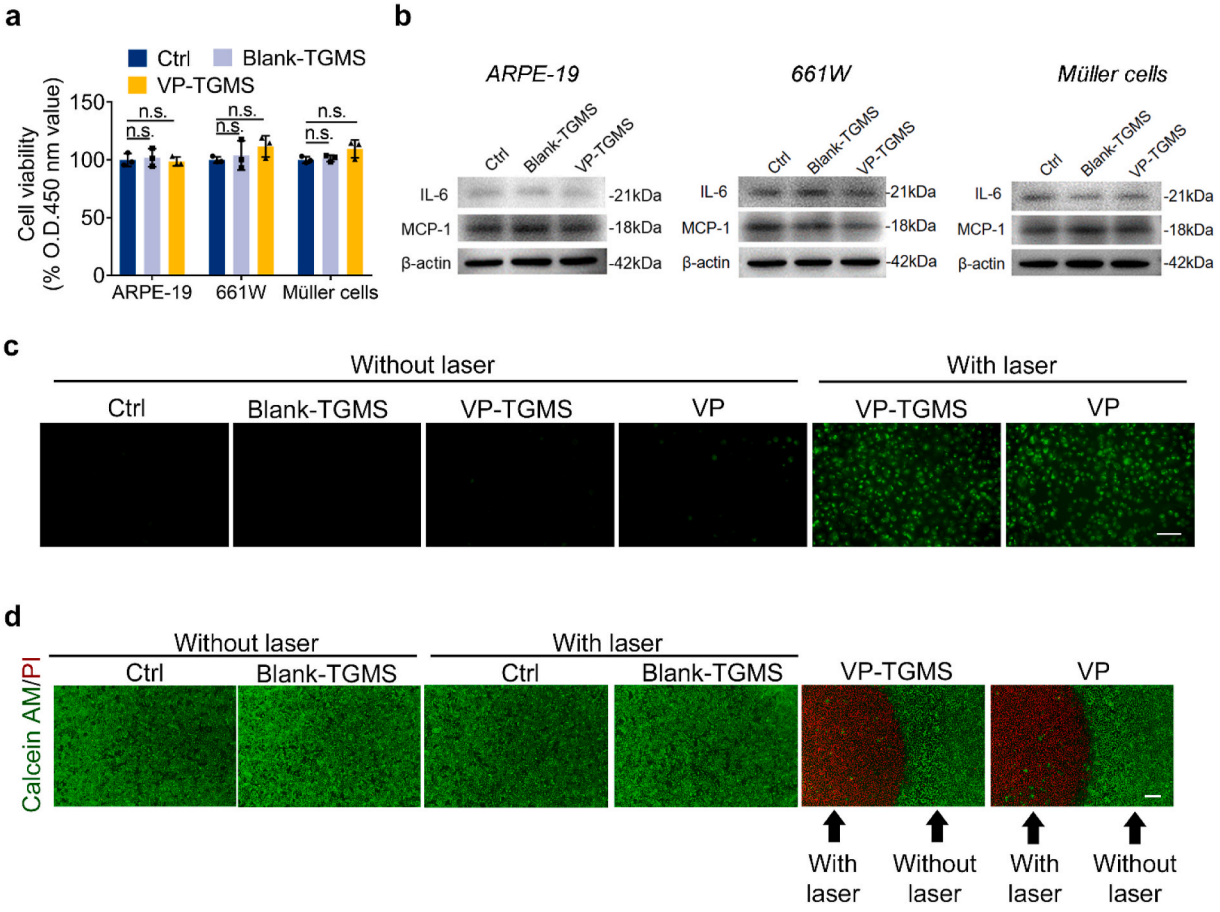

Fig. 3. *In vitro* biocompatibility and photodynamic effects of VP-TGMS. **(a)** Viability of ARPE-19 cells, 661W cells and Müller cells treated with Blank-TGMS or VP-TGMS hydrogels as detected by CCK-8 assay (n = 3), n.s.: no statistical significance. **(b)** Protein expression levels of the inflammatory cytokines IL-6 and MCP-1 in ARPE-19 cells, 661W cells and Müller cells treated with Blank-TGMS or VP-TGMS hydrogels. **(c)** Detection of $^1O_2$ generation using singlet oxygen fluorescent probes which reacted with $^1O_2$ to generate green fluorescence substance. Scale bar: 50 μm. **(d)** Representative images by live/dead staining of HUVECs incubated in medium or medium with VP, Blank TGMS or VP-TGMS hydrogels added to the culture inserts. Live cells were stained with calcein AM and dead cells were stained with PI. Scale bar: 200 μm.

free VP on HUVECs under laser activation, we chose 4 μM of VP as a positive control (Fig. S3). $^1O_2$ fluorescent probes can react with $^1O_2$ to generate a green fluorescence substance accumulated in the cells. As shown in Fig. 3c, no obvious fluorescence generation was detected in HUVECs incubated with normal medium, Blank-TGMS, VP-TGMS or VP without laser irradiation, while a significant enhancement in fluorescence was observed in VP-TGMS- and VP-treated cells after laser exposure. To further assess the phototoxic effects of VP-TGMS, live/dead

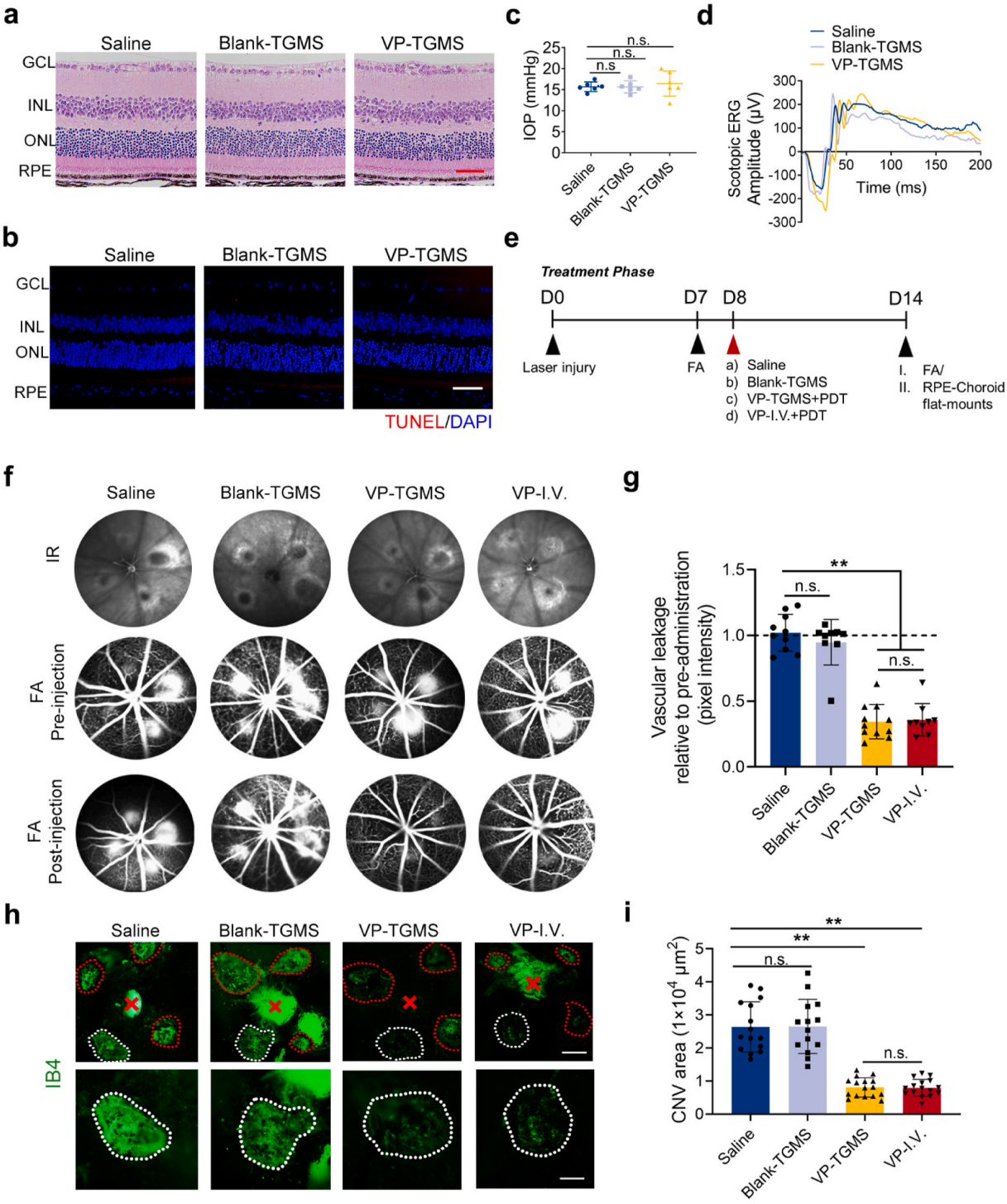

Fig. 4. *In vivo* biocompatibility and photodynamic effects of VP-TGMS. **(a)** Representative retinal images after injection of Blank-TGMS and VP-TGMS hydrogels by H&E staining. Scale bar: 50 μm. **(b)** Representative retinal images after injection of Blank-TGMS and VP-TGMS hydrogels by TUNEL staining. Scale bar: 50 μm. **(c)** IOP measurement one day after injection (n = 6). **(d)** Scotopic ERG responses of mice 7 days after each treatment. **(e)** Diagram of the schedule for laser injury, different therapeutic treatments and FA analyses/IB4 staining. **(f)** Representative infrared (IR) fundus images and FA images presenting choroidal neovascular leakage of eyes pre- and post-injection. **(g)** Quantification of the fluorescence pixel intensity of the neovascular leakage area (n = 9–11). **P < 0.01 by one-way ANOVA followed by LSD post hoc test, n.s.: no statistical significance. **(h)** Representative IB4-stained CNV lesions in eyes with different treatments. Scale bars: 200 μm (upper panel), 100 μm (lower panel). **(i)** Quantification of the CNV area (n = 14–16 lesions). **P < 0.01 by one-way ANOVA followed by LSD post hoc test, n.s.: no statistical significance.

staining was performed using calcein-AM/PI probes. Notably, there was a clear line deviding the laser-targeted area and the non-irradiated area to distinguish dead cells from live cells, providing direct evidence of the excellent targeting ability and photodynamic efficiency of VP-TGMS treatment (Fig. 3d). The unchanged cell viability in the area without light irradiation in the VP-TGMS group further verified the good biocompatibility of the VP-TGMS gels. Additionally, our data showed that VP-TGMS co-incubated with HUVECs within 24 h did release VP with an effective concentration of photodynamic effect. Notably, VP-TGMS gels released more VP with HUVECs co-incubation for 24 h compared to VP-TGMS in the absence of HUVECs (4.91 ± 0.17% *vs.* 3.61 ± 0.36%) ($p = 0.0047$) (Fig. S4), possibly because HUVECs can autocrine cytokines including MMPs [43], thereby disassemble VP-TGMS gels.

3.4. *In vivo* biocompatibility and photodynamic effects of VP-TGMS

Although many patients benefit from PDT through either CVDs treatment or tumor treatment, one concern that has resulted from this traditional way of delivering large doses of a photosensitizer drug intravenously is poor patient compliance [44]. In addition, systemic administration is associated with a high health requirement of the systemic system of patients, thus increasing the proportion of the population that is not eligible for this type of therapy. This mode of administration increases the risk of systemic adverse effects from photosensitizers [13]. Therefore, we propose a new strategy to ameliorate these problems with the existing therapies. Having demonstrated that VP-TGMS hydrogels have good biocompatibility and photodynamic efficiency *in vitro*, we investigated the effects of this in situ gelation-based VP-PDT strategy *in vivo*. First, *in vivo* biocompatibility evaluation was performed. After administration, the mice were kept under a standard lighting regimen (15–20 lx). As assessed by hematoxylin and eosin (H&E) histology (Fig. 4a) and TUNEL staining (Fig. 4b), mice intravitreally injected with Blank-TGMS and VP-TGMS hydrogels showed no significant structural abnormalities or cytotoxicity in the posterior segments 7 days after treatment. Furthermore, mice treated with hydrogels had normal intraocular pressure (IOP) (Fig. 4c) and electroretinogram (ERG) responses (Fig. 4d), which was consistent with the intravitreal injection of saline, further indicating that intravitreal injection of VP-TGMS hydrogels would not lead to abnormalities in retinal morphology or visual function. To recreate a clinical scenario, the VP-I.V. (intravenous injection of VP) group was used as a positive control. H&E staining of the main organs of the mice that received intravitreal injection of VP-TGMS hydrogels or intravenous injection of VP for 2 weeks showed no noticeable organ injury, inflammatory cell invasion or other pathological responses compared to the control group (Fig. S5). Biodegradability is a necessary characteristic for intraocular drug delivery carriers. We then evaluated the capacity of the TGMS hydrogel for subcutaneous degradation in nude mice. The results showed that 100 μL of the TGMS gel gradually degraded *in vivo* over 8 weeks (Fig. S6). Taken together, these results show that TGMS has excellent *in vivo* biocompatibility and biodegradability, which may provide an important basis for potential clinical translation.

To investigate the photodynamic therapeutic effects of intravitreal injection of the VP-TGMS hydrogels, we established a laser-induced CNV mouse model, which has been widely used to evaluate the efficacy of treatment for CVDs [45]. Endowed with alterative capillary structures and morphology, neovessels are characterized by hyperpermeability that leads to neovascular leakage [46]. On Day 7 after laser photocoagulation, fluorescein angiography (FA) was performed to record vascular leakage before administration. On Day 8, the mice were administered different treatments, and FA images were obtained again 7 days after treatment to evaluate the photodynamic effects of the VP-TGMS hydrogels on choroidal neovascular permeability (Fig. 4e). Consistent with pre-injection, saline-treated and Blank-TGMS-treated mice showed prominent vascular leakage after injection (Fig. 4f). Notably, under light-on conditions, mice with VP-TGMS treatment and VP-I.V. treatment showed markedly attenuated vascular leakage (both $p < 0.0001$), indicating that the light had activated VP and had effectively occluded the leaky vessels (Fig. 4f and g). Subsequently, the photodynamic effects of the VP-TGMS hydrogels were assessed by isolectin B4 (IB4, a biomarker of neovessels) staining of RPE/choroid flat mounts. The size of the newly generated CNV was evaluated by measuring the fluorescence intensity. As shown in Fig. 4h, eyes treated with VP-TGMS showed a marked reduction in the CNV lesion area by 69.34% ($p < 0.0001$), which was comparable to the therapeutic effect observed after intravenous injection of VP (69.86%, $p < 0.0001$) (Fig. 4i), further suggesting the effectiveness and specificity of photoactivated VP-TGMS in inhibiting neovascular lesions. The main mechanism by which VP targets the ECs during pathological neovascularization is to recognize the highly expressed low-density lipoprotein (LDL) receptor in ECs of neovessels by combining with LDL in the blood. However, it has been reported that other mechanisms of VP cellular uptake may also be involved *in vivo* [10]. Due to the abnormal structure of neovessels, small molecule drugs, especially lipophilic agents such as VP, could be readily absorbed by ECs through the mediation of the neovascular hyperpermeability of the impaired blood-retinal barrier [9], which explains the underlying therapeutic mechanism of the VP-TGMS drug delivery system in this study. By further introducing the properties of this system, a local VP-TGMS therapeutic strategy allowed VP microdosing at the lesion site. Compared to the clinical dosage of 6 mg/m^2 (body surface area) for systemic administration [10], the dose of VP for local administration could be largely reduced and still reach an effective drug concentration, which consequently reduces costs and avoids systemic photosensitive reactions.

3.5. *In vitro* inhibitory effects of the non-photoactivated VP-TGMS on VEGF-induced angiogenesis

Although the efficacy of PDT for CVDs treatment in the clinic is encouraging [16,47] and our experiments confirmed the excellent efficacy of VP-PDT in inhibiting vascular leakage, the strategy presented herein remains a temporary solution and does not reflect a permanent cure because of the sustained release of VEGF. VEGF is the core regulator and clinical therapeutic target for neovascularization in patients with fundus neovascular diseases [7]. PDT alone cannot inhibit the tendency of angiogenesis induced by the intraocular high-VEGF environment [48]. Notably, VP is not only a photosensitizer but also a potent inhibitor of YAP, the core regulator of Hippo signaling, which is a highly conserved pathway involved in developmental processes, including organ size control and tissue regeneration [49]. Non-photoactivated VP can inhibit YAP transcriptional activation to hamper downstream gene transcription [50]. It has been found that non-photodynamic VP has a tumor suppressive effect, and investigators have considered this effect to be linked to its antivascular effects [51,52]. In addition, an active change in the expression of YAP was also observed on the developing front of neovessels including ocular vessels [53,54], implying that YAP is a potential regulator of ocular angiogenesis. However, the underlying role of non-photoactive VP in ocular neovascularization remains to be elucidated. Herein, we sought to investigate the effects of non-photoactive VP-TGMS to regulate VEGF-induced angiogenic responses in ECs. EC migration and tube formation are crucial steps in the process of pathological neovascularization. *In vitro* experiments, including Transwell assays, scratch assays and Matrigel tube formation assays, were then carried out. After treatment with VEGF, HUVECs displayed enhanced migration compared to cells under basal conditions, while the EC migration capacity was remarkably compromised with the addition of 4 μM of VP, which was consistent with a previous study [51]. Similarly, a significant increase in migration was observed in cells incubated with the Blank-TGMS gels in VEGF-supplemented medium. After treatment with VP-TGMS hydrogels under light-off conditions, the vertical and lateral migration capacity of HUVECs was blunted ($p =$

0.0274 and $p = 0.0095$ versus Blank-TGMS, respectively) (Fig. 5a–d), and in response to lipase, the VP released from the VP-TGMS gels aggravated the inhibitory effect on the vertical and lateral migration ($p = 0.0047$ and $p < 0.0001$ versus Blank-TGMS, respectively) (Fig. 5a–d). Consistently, the VEGF-induced formation of EC tubes was significantly restrained by free VP or VP from the VP-TGMS gels, as quantified by the number of tubes, branches and nodes (both $p < 0.0001$) (Fig. 5e and f). We found that free VP inhibited the VEGF-induced angiogenic response beyond that of the control group. A possible reason may be that HUVECs in the control group spontaneously secreted VEGF to maintain cell growth, and non-photoactive VP inhibited angiogenic responses induced by both endogenous and exogenous VEGF *in vitro*.

3.6. *In vivo antiangiogenic effects of VP-TGMS in a laser-induced CNV model under light-off conditions*

Given that the non-photoactivated VP-TGMS hydrogels could inhibit VEGF-induced angiogenic responses *in vitro*, we further investigated their effects in a laser-induced CNV mouse model under light-off conditions. Laser photocoagulation was performed to generate the CNVs. Subsequently, mice were treated with (A) saline, (B) Blank-TGMS, (C) VP-TGMS or (D) VP (intravenous injection). The mice were then kept under a standard lighting regimen (15–20 lx) without laser activation. FA was performed 7 days after administration (Fig. 6a). Compared to saline treatment, VP-TGMS treatment significantly reduced fluorescein leakage ($p = 0.0002$), while there was no significant suppression of leakage in the mice treated with Blank-TGMS or systemic VP ($p = 0.9766$ and $p = 0.8206$, respectively) (Fig. 6b and c). We further confirmed these findings by monitoring neovascularization with IB4-stained flat mounts, which showed that the VP-TGMS hydrogels could effectively decrease the size of the CNV lesions ($p < 0.0001$) (Fig. 6d and e). The effects of non-photoactivated VP and photoactivated VP on vascular leakage inhibition were similar by FA analysis. However, we found a clear distinction between the two on the IB4-stained flat mounts. PDT is the effect of phototoxicity-induced neovascular occlusion. Therefore, the decrease in the fluorescence positive rate from IB4 was shown on the flat mounts at the laser spot position. However, the non-photoactivated VP inhibited angiogenesis, so that newly formed CNVs embodied in IB4 staining were relatively small in overall size. For comparison, intravenous injection of non-photoactive VP did not inhibit CNV formation (p

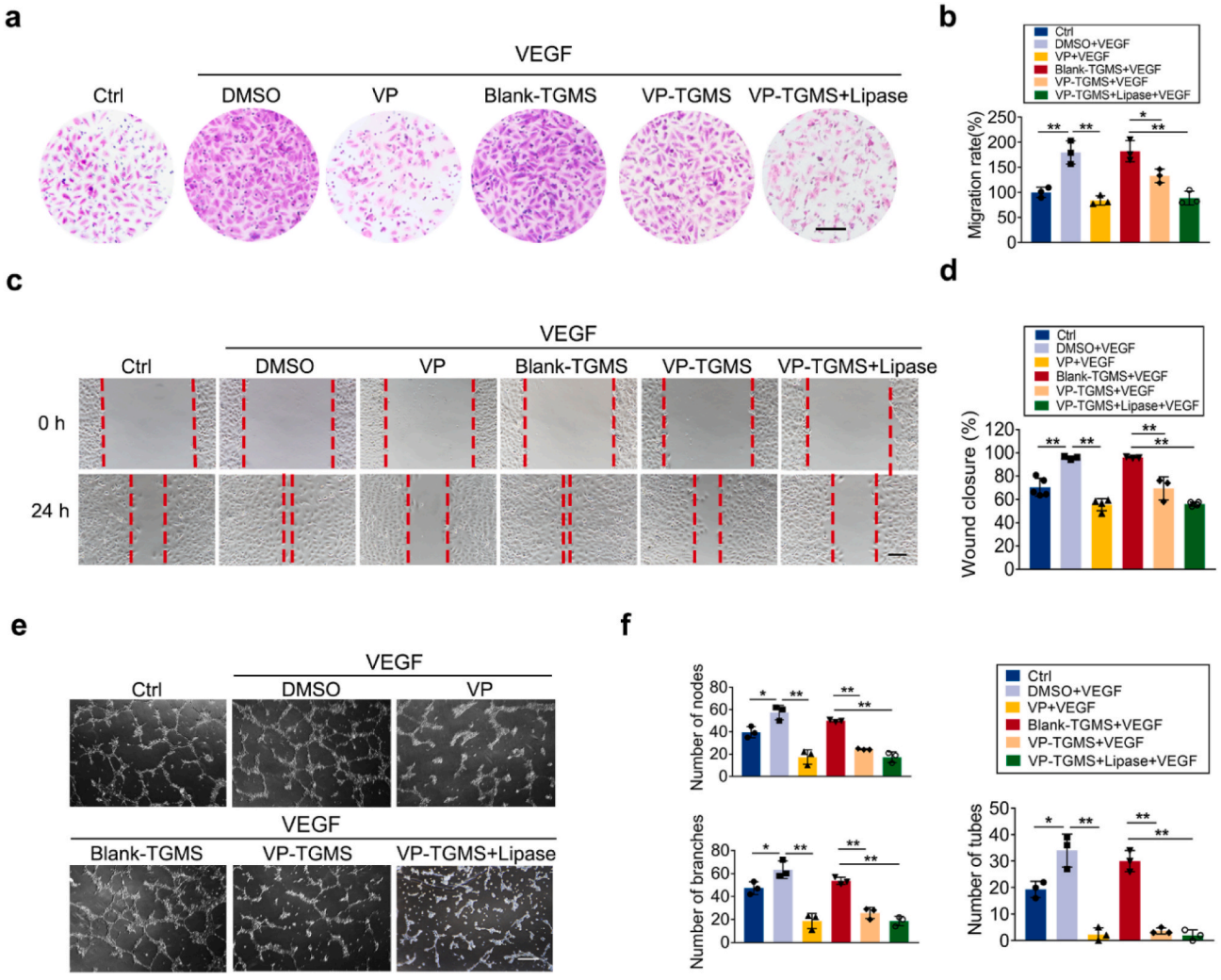

Fig. 5. VEGF-induced angiogenic responses were inhibited by non-photoactive VP-TGMS. **(a)** Vertical migration of HUVECs in response to each treatment by Transwell assay. Scale bar: 100 μm. **(b)** The number of migrated cells on the lower surface of the culture inserts was counted, and the data were normalized according to the control group (n = 3). *P < 0.05, **P < 0.01 by one-way ANOVA followed by LSD post hoc test. **(c)** Lateral migration of HUVECs was determined by a scratch assay after 24 h. Scale bar: 100 μm. **(d)** The migration rate was quantified by calculating the wound healing (% closure) of the scratch area (n = 3). *P < 0.05, **P < 0.01 by one-way ANOVA followed by LSD post hoc test. **(e)** Representative images of HUVEC network formation after different treatments from the Matrigel tube formation assay. Scale bar: 200 μm. **(f)** Quantification of nodes, branches and tube numbers from three independent tube formation experiments (n = 3). *P < 0.05, **P < 0.01 by one-way ANOVA followed by LSD post hoc test.

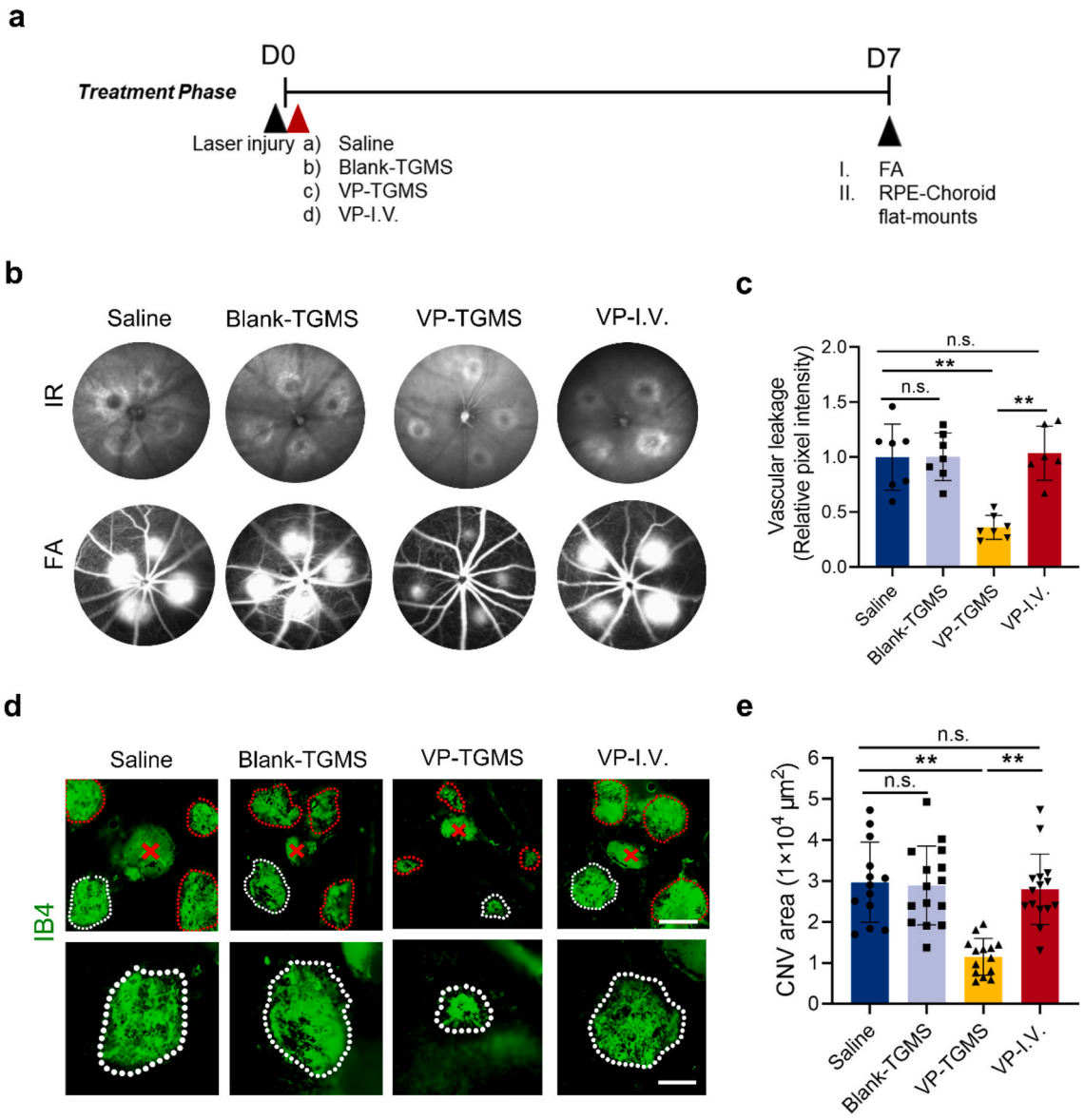

Fig. 6. Non-photoactive VP-TGMS inhibits CNV formation and vascular leakage. **(a)** Diagram of the schedule for laser injury, the different therapeutic treatments and FA analysis/IB4 staining. **(b)** Representative IR fundus images and FA images presenting eye choroidal neovascular leakage post-administration. **(c)** Quantification of the fluorescence pixel intensity of the neovascular leakage area (n = 6–7). **P < 0.01 by one-way ANOVA followed by LSD post hoc test, n.s.: no statistical significance. **(d)** Representative IB4-stained CNV lesions in eyes after different treatments. Scale bars: 200 μm (upper panel), 100 μm (lower panel). **(e)** Quantification of CNV area (n = 13–15 lesions). Error bars represent the means ± SD. **P < 0.01 by one-way ANOVA followed by LSD post hoc test, n.s.: no statistical significance.

= 0.6291) (Fig. 6d and e), further demonstrating that the sustained release of non-photoactive VP from the VP-TGMS hydrogels could remarkably inhibit neovascularization. We supposed that free VP might have been eliminated from the body due to its short half-life of 2–3 h [52] in systemic circulation before being able to steadily exert its YAP inhibitory effects.

3.7. Mechanistic analysis of the antiangiogenic activity of the non-photoactivated VP

To gain further insight into the ability of VP to inhibit the angiogenic process without light activation, we performed transcriptomic analyses of VEGF-treated HUVECs with or without VP pre-incubation. Among the top 40 significantly changed genes identified by RNA sequencing (RNA-seq), the expression levels of 3 genes involved in the negative regulation of angiogenesis (i.e., *GADD45A, NRG1, WARS1*) increased and 6 genes involved in the positive regulation of angiogenesis (i.e., *CAV1, TNFAIP2, JUP, SHH, ITGAV, EFNA1*) decreased after VP treatment (Fig. 7a). Additionally, gene set enrichment analysis (GSEA) was performed to assess the biological processes enriched from Gene Ontology (GO) terms. Compared to the VEGF group, genes associated with the biological processes contributing to the initiation of sprouting angiogenesis (including cell adhesion, cell migration, ECM organization and ECM disassembly) were significantly decreased after VP treatment (Fig. S7), showing that non-photoactive VP had a biological effect on inhibiting angiogenic activities. Additionally, enrichment analysis of the down-regulated genes in VEGF + VP group from Reactome database (https://reactome.org/) revealed a robust correlation in VEGF-related signaling, further providing evidence that YAP inhibition by non-photoactive VP could downregulate proangiogenic gene transcription from VEGF signaling (Fig. 7b). Hippo-YAP signaling pathway is involved in terminal organ development, and angiogenesis is such an inextricable part of organ development. Our results demonstrated that there was an underlying crosstalk between VEGF and Hippo-YAP signaling pathway

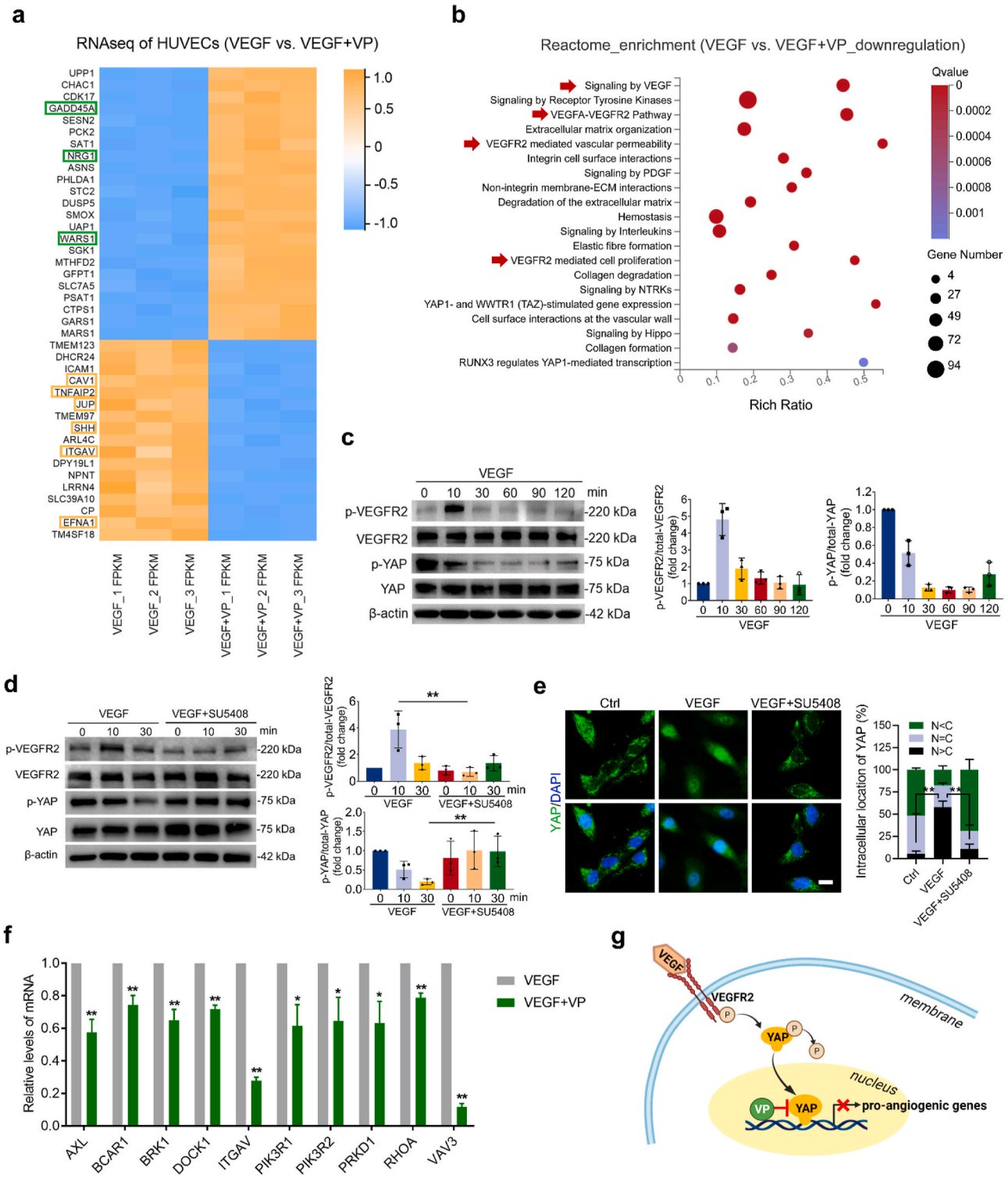

Fig. 7. VP inhibits VEGF-induced VEGFR2-YAP signaling. **(a)** Heatmap showing RNA-seq expression of the top 40 marker genes identified from VEGF-treated HUVECs and VEGF + VP-treated HUVECs. Green box: genes that negatively regulate angiogenesis, yellow box: genes that positively regulate angiogenesis. **(b)** Reactome enrichment analysis of downregulated genes in HUVECs treated with VEGF + VP compared with VEGF-treated cells. The red arrowhead indicates biological processes related to VEGF-VEGFR2 signaling. **(c)** Western blotting detection and quantification of VEGFR2 phosphorylation and YAP phosphorylation in HUVECs incubated with VEGF (200 ng/mL) for the indicated time points (n = 3). **(d)** VEGFR2 phosphorylation and YAP phosphorylation in HUVECs pretreated with or without SU5408 (a VEGFR2 kinase inhibitor) and then incubated with VEGF for the indicated lengths of time (n = 3). **P < 0.01 by Student's *t*-test. **(e)** Subcellular localization and quantification of YAP in HUVECs pretreated with SU5408 for 2 h and then stimulated with VEGF for 6 h, as illustrated by immunofluorescence (n = 3). N: nucleus, C: cytosol. Scale bar: 10 μm **P < 0.01 by one-way ANOVA followed by LSD post hoc test. **(f)** qPCR validation of the mRNA expression of genes related to the VEGF receptor signaling pathway identified by RNA-seq in HUVECs (n = 3). *P < 0.05, **P < 0.01 by Student's *t*-test. **(g)** Schematic depiction of VP inhibition of the VEGFR2-YAP signaling axis.

during angiogenesis, which is also supported by recent studies [19,22,55,56]. Based on the results of RNA-seq analysis, we next monitored the phosphorylation of VEGFR2 (the cognate receptor of VEGF) and YAP upon VEGF stimulation by western blot analysis. YAP phosphorylation leads to cytoplasmic degradation of YAP [57]. When YAP is dephosphorylated, YAP translocates to the nucleus, which results in the activation of YAP signaling [58]. VEGFR2 activation peaked at 10 min after VEGF treatment, while YAP dephosphorylation was observed at 30 min (Fig. 7c), indicating that YAP activation could be initiated by VEGF. To understand whether VEGF-mediated YAP activation was regulated via VEGFR2 signaling, we further treated VEGF-incubated HUVECs with a VEGFR2 kinase inhibitor (SU5408). Under treatment with this VEGFR2 inhibitor, neither dephosphorylation (Fig. 7d) nor nuclear translocation (Fig. 7e) of YAP was observed, suggesting that activation of the VEGF-VEGFR2 pathway can intimately regulate the transcriptional activity of YAP. We further confirmed that VP treatment downregulated the expression levels of VEGFR2-related signaling target genes by qPCR analysis (Fig. 7f), which revealed that YAP inhibition by VP indeed hampered the activation of VEGF-VEGFR2 signaling (Fig. 7g). Clinically, *anti*-VEGF agents are first-line medication for the treatment of CVDs. However, some patients, especially those with PCV, do not respond to *anti*-VEGF treatment [59,60]. A possible reason is that the transduction of signal pathways is often not linear in complex *in vivo* environments. The VEGFR2 signaling pathway involves the intricate crosstalk of other signaling pathways, including the Hippo-YAP pathway. Upstream proteins of VEGFR2 signaling can be input by additional signals, thus affecting the downstream final outcome [61]. With YAP being a transcriptional endpoint of the VEGFR2 signaling pathway, the effects of its inhibition by non-photoactive VP may be more direct. In addition, clinical studies have shown that the combined treatment of inhibiting VEGF and PDT brings more significant therapeutic effect for some types of CVDs [11,16]. According to the concept we designed here, our system can serve as an intraocular drug reservoir that avoids the rapid elimination of VP from the ocular space to achieve synergistic inhibitory effects on pathological angiogenesis.

In summary, the present study demonstrated the efficacy of an in-situ VP delivery system to inhibit neovascularization under both light-on (laser-dependent) and light-off (laser-independent) conditions. The combination of the PDT-mediated effects and YAP inhibitory effects of VP-TGMS significantly boosts antiangiogenic activity via symptomatic treatment and etiological treatment.

4. Conclusion

Photodynamic sealing of pathological neovessels combined with sustained inhibition of VEGF-induced angiogenesis represents a promising approach to improve the clinical treatment of CVDs. In this study, we developed an in situ VP-loaded delivery strategy with synergistic inhibitory effects on neovascularization under both light-on and light-off conditions. VP was released from the VP-TGMS hydrogels in response to MMP-2/9 in the pathological milieus of CVDs. Under light-on conditions, VP acts as a photosensitizer and triggers oxidative damage in abnormal ECs by producing ROS, leading to vascular occlusion. Under light-off conditions, as a potent YAP inhibitor, the sustained non-photoactive VP released from VP-TGMS hampers VEGF-induced angiogenesis by regulating the transcriptional inhibition of angiogenic genes. Taken together, via the dual mechanisms of VP, our gelation-based therapy not only alleviated the symptoms but also aimed at the molecular cause of neovascularization, producing a novel additive and synergistic treatment for choroid vascular diseases. More broadly, this effective, efficient and economical therapeutic strategy may be extended to applications in other neovascular diseases with inflammatory milieu such as oncology, thus providing a viable alternative to the current conventional PDT strategy.

Data availability

All data used to evaluate the conclusions in the paper are presented in the paper and the Supplementary Materials. The raw RNA-seq data reported in this study have been deposited in the Gene Expression Omnibus database with accession number (GSE181880). Additional data related to this paper are available from the corresponding author upon any reasonable request.

CRediT authorship contribution statement

Yahan Ju: Methodology, Investigation, Writing – original draft. **Xiaochan Dai:** Methodology, Investigation, Writing – original draft. **Zhimin Tang:** Methodology, Investigation. **Zunzhen Ming:** Validation, Visualization. **Ni Ni:** Validation, Investigation. **Dongqing Zhu:** Resources, Supervision, Data curation. **Jing Zhang:** Resources, Supervision, Data curation. **Bo Ma:** Resources, Supervision, Data curation. **Jiajing Wang:** Formal analysis, Visualization. **Rui Huang:** Formal analysis, Visualization. **Siyu Zhao:** Formal analysis, Visualization. **Yan Pang:** Conceptualization, Writing – review & editing, Funding acquisition, Supervision. **Ping Gu:** Conceptualization, Writing – review & editing, Funding acquisition, Supervision.

Declaration of competing interest

The authors declare that they have no competing interests.

Acknowledgments

This work was supported by the National Natural Science Foundation of China (81870687, 82071004, 32000972), the National Key R&D program of China (2018YFC1106100), the Key program of Shanghai Science and Technology Commission (19JC1415503), and the Municipal Education Commission-Gaofeng Clinical Medicine Grant Support (20161316, 20191820), Cross-disciplinary Research Fund of Shanghai Ninth People's Hospital, Shanghai Jiao Tong University School of Medicine (No. JYJC201907) and Science and Technology Commission of Shanghai (20DZ2270800).

Appendix A. Supplementary data

Supplementary data to this article can be found online at https://doi.org/10.1016/j.bioactmat.2022.01.028.

References

[1] J. Brinks, E.H.C. van Dijk, I. Klaassen, R.O. Schlingemann, S.M. Kielbasa, E. Emri, et al., Exploring the choroidal vascular labyrinth and its molecular and structural roles in health and disease, Prog. Retin. Eye Res. (2021) 100994.
[2] E. Borrelli, D. Sarraf, K.B. Freund, S.R. Sadda, OCT angiography and evaluation of the choroid and choroidal vascular disorders, Prog. Retin. Eye Res. 67 (2018) 30–55.
[3] R. Agrawal, J. Ding, P. Sen, A. Rousselot, A. Chan, L. Nivison-Smith, et al., Exploring choroidal angioarchitecture in health and disease using choroidal vascularity index, Prog. Retin. Eye Res. 77 (2020) 100829.
[4] C.W. Wong, Y. Yanagi, W.K. Lee, Y. Ogura, I. Yeo, T.Y. Wong, et al., Age-related macular degeneration and polypoidal choroidal vasculopathy in Asians, Prog. Retin. Eye Res. 53 (2016) 107–139.
[5] P.A. Campochiaro, A. Akhlaq, Sustained suppression of VEGF for treatment of retinal/choroidal vascular diseases, Prog. Retin. Eye Res. (2020) 100921.
[6] P. Mitchell, G. Liew, B. Gopinath, T.Y. Wong, Age-related macular degeneration, Lancet 392 (10153) (2018) 1147–1159.
[7] P.A. Campochiaro, Molecular pathogenesis of retinal and choroidal vascular diseases, Prog. Retin. Eye Res. 49 (2015) 67–81.
[8] L. Garcia-Onrubia, F.J. Valentin-Bravo, R.M. Coco-Martin, R. Gonzalez-Sarmiento, J.C. Pastor, R. Usategui-Martin, et al., Matrix metalloproteinases in age-related macular degeneration (AMD), Int. J. Mol. Sci. 21 (16) (2020).
[9] M. Battaglia Parodi, C. La Spina, L. Berchicci, G. Petruzzi, F. Bandello, Photosensitizers, Photodynamic Therapy, Verteporfin, Dev. Ophthalmol. 55 (2016) 330–336.

[10] U. Schmidt-Erfurth, T. Hasan, Mechanisms of action of photodynamic therapy with verteporfin for the treatment of age-related macular degeneration, Surv. Ophthalmol. 45 (3) (2000) 195–214.
[11] A. Koh, T.Y.Y. Lai, K. Takahashi, T.Y. Wong, L.J. Chen, P. Ruamviboonsuk, et al., Efficacy and safety of ranibizumab with or without verteporfin photodynamic therapy for polypoidal choroidal vasculopathy: a randomized clinical trial, J. AM. A. Ophthalmol. 135 (11) (2017) 1206–1213.
[12] M. Azab, M. Benchaboune, K.J. Blinder, N.M. Bressler, S.B. Bressler, E. S. Gragoudas, et al., Verteporfin therapy of subfoveal choroidal neovascularization in age-related macular degeneration: meta-analysis of 2-year safety results in three randomized clinical trials: treatment of Age-Related Macular Degeneration with Photodynamic Therapy and Verteporfin in Photodynamic Therapy Study Report no. 4, Retina 24 (1) (2004) 1–12.
[13] U.E. Schnurrbusch, C. Jochmann, W. Einbock, S. Wolf, Complications after photodynamic therapy, Arch. Ophthalmol. 123 (10) (2005) 1347–1350.
[14] Guidelines for using verteporfin (visudyne) in photodynamic therapy to treat choroidal neovascularization due to age-related macular degeneration and other causes, Retina 22 (1) (2002) 6–18.
[15] A. Koh, W.K. Lee, L.J. Chen, S.J. Chen, Y. Hashad, H. Kim, et al., EVEREST study: efficacy and safety of verteporfin photodynamic therapy in combination with ranibizumab or alone versus ranibizumab monotherapy in patients with symptomatic macular polypoidal choroidal vasculopathy, Retina 32 (8) (2012) 1453–1464.
[16] T.H. Lim, T.Y.Y. Lai, K. Takahashi, T.Y. Wong, L.J. Chen, P. Ruamviboonsuk, et al., Comparison of ranibizumab with or without verteporfin photodynamic therapy for polypoidal choroidal vasculopathy: the EVEREST II randomized clinical trial, J. AM. A. Ophthalmol. 138 (9) (2020) 935–942.
[17] J. Baek, J.H. Lee, W.K. Lee, Clinical relevance of aqueous vascular endothelial growth factor levels in polypoidal choroidal vasculopathy, Retina 37 (5) (2017) 943–950.
[18] J.R. Misra, K.D. Irvine, The Hippo signaling network and its biological functions,, Annu. Rev. Genet. 52 (2018) 65–87.
[19] H.H. Pulkkinen, M. Kiema, J.P. Lappalainen, A. Toropainen, M. Beter, A. Tirronen, et al., BMP6/TAZ-Hippo signaling modulates angiogenesis and endothelial cell response to VEGF, Angiogenesis 24 (1) (2021) 129–144.
[20] X. Zhu, Y. Shan, M. Yu, J. Shi, L. Tang, H. Cao, et al., Tetramethylpyrazine ameliorates peritoneal angiogenesis by regulating VEGF/Hippo/YAP signaling, Front. Pharmacol. 12 (2021) 649581.
[21] J. Kim, Y.H. Kim, J. Kim, D.Y. Park, H. Bae, D.H. Lee, et al., YAP/TAZ regulates sprouting angiogenesis and vascular barrier maturation, J. Clin. Invest. 127 (9) (2017) 3441–3461.
[22] T. Azad, H.J. Janse van Rensburg, E.D. Lightbody, B. Neveu, A. Champagne, A. Ghaffari, et al., A LATS biosensor screen identifies VEGFR as a regulator of the Hippo pathway in angiogenesis, Nat. Commun. 9 (1) (2018) 1061.
[23] R.C. Cooper, H. Yang, Hydrogel-based ocular drug delivery systems: emerging fabrication strategies, applications, and bench-to-bedside manufacturing considerations, J. Contr. Release 306 (2019) 29–39.
[24] C.R. Lynch, P.P.D. Kondiah, Y.E. Choonara, L.C. du Toit, N. Ally, V. Pillay, Hydrogel biomaterials for application in ocular drug delivery, Front. Bioeng. Biotechnol. 8 (2020) 228.
[25] S. Kirchhof, A.M. Goepferich, F.P. Brandl, Hydrogels in ophthalmic applications, Eur. J. Pharm. Biopharm. 95 (2015) 227–238. Pt B.
[26] A. Lommatzsch, P. Hermans, K.D. Muller, N. Bornfeld, A.C. Bird, D. Pauleikhoff, Are low inflammatory reactions involved in exudative age-related macular degeneration? Morphological and immunhistochemical analysis of AMD associated with basal deposits, Graefes Arch. Clin. Exp. Ophthalmol. 246 (6) (2008) 803–810.
[27] S. Hoffmann, S. He, M. Ehren, S.J. Ryan, P. Wiedemann, D.R. Hinton, MMP-2 and MMP-9 secretion by rpe is stimulated by angiogenic molecules found in choroidal neovascular membranes, Retina 26 (4) (2006) 454–461.
[28] J.J. Plantner, C. Jiang, A. Smine, Increase in interphotoreceptor matrix gelatinase A (MMP-2) associated with age-related macular degeneration, Exp. Eye Res. 67 (6) (1998) 637–645.
[29] S.R. Shah, J. Kim, P. Schiapparelli, C.A. Vazquez-Ramos, J.C. Martinez-Gutierrez, A. Ruiz-Valls, et al., Verteporfin-loaded polymeric microparticles for intratumoral treatment of brain cancer, Mol. Pharm. 16 (4) (2019) 1433–1443.
[30] Y. Ju, Z. Tang, X. Dai, H. Gao, J. Zhang, Y. Liu, et al., Protection against light-induced retinal degeneration via dual anti-inflammatory and anti-angiogenic functions of thrombospondin-1, Br. J. Pharmacol. (2020).
[31] A. Odergren, Y. Ming, A. Kvanta, Photodynamic therapy of experimental choroidal neovascularization in the mouse, Curr. Eye Res. 31 (9) (2006) 765–774.
[32] D.N. Zacks, E. Ezra, Y. Terada, N. Michaud, E. Connolly, E.S. Gragoudas, et al., Verteporfin photodynamic therapy in the rat model of choroidal neovascularization: angiographic and histologic characterization, Invest. Ophthalmol. Vis. Sci. 43 (7) (2002) 2384–2391.
[33] Z. Tang, M. Huo, Y. Ju, X. Dai, N. Ni, Y. Liu, et al., Nanoprotection against retinal pigment epithelium degeneration via ferroptosis inhibition, Small Methods 5 (12) (2021), e2100848.
[34] Z. Tang, Y. Ju, X. Dai, N. Ni, Y. Liu, D. Zhang, et al., HO-1-mediated ferroptosis as a target for protection against retinal pigment epithelium degeneration, Redox Biol. 43 (2021) 101971.
[35] P. Baranowski, B. Karolewicz, M. Gajda, J. Pluta, Ophthalmic drug dosage forms: characterisation and research methods, Sci. World J. (2014) 861904, 2014.
[36] J. Kokavec, S.H. Min, M.H. Tan, J.S. Gilhotra, H.S. Newland, S.R. Durkin, et al., Biochemical analysis of the living human vitreous, Clin. Exp. Ophthalmol. 44 (7) (2016) 597–609.
[37] J. Kurzepa, A. Mądro, G. Czechowska, J. Kurzepa, K. Celiński, W. Kazmierak, et al., Role of MMP-2 and MMP-9 and their natural inhibitors in liver fibrosis, chronic pancreatitis and non-specific inflammatory bowel diseases, Hepatobiliary Pancreat. Dis. Int. 13 (6) (2014) 570–579.
[38] N. Mansoor, F. Wahid, M. Azam, K. Shah, A.I. den Hollander, R. Qamar, et al., Molecular mechanisms of complement system proteins and matrix metalloproteinases in the pathogenesis of age-related macular degeneration, Curr. Mol. Med. 19 (10) (2019) 705–718.
[39] Y. Tian, F. Zhang, Y. Qiu, S. Wang, F. Li, J. Zhao, et al., Reduction of choroidal neovascularization via cleavable VEGF antibodies conjugated to exosomes derived from regulatory T cells, Nat Biomed Eng. 5 (9) (2021) 968–982.
[40] S.B. Bressler, Introduction: understanding the role of angiogenesis and antiangiogenic agents in age-related macular degeneration, Ophthalmol. 116 (10 Suppl) (2009). S1–7.
[41] H. Ghasemi, Roles of IL-6 in ocular inflammation: a review, Ocul. Immunol. Inflamm. 26 (1) (2018) 37–50.
[42] W. Raoul, C. Auvynet, S. Camelo, X. Guillonneau, C. Feumi, C. Combadière, et al., CCL2/CCR2 and CX3CL1/CX3CR1 chemokine axes and their possible involvement in age-related macular degeneration, J. Neuroinflammation 7 (2010) 87.
[43] C.J. Jackson, M. Nguyen, Human microvascular endothelial cells differ from macrovascular endothelial cells in their expression of matrix metalloproteinases, Int. J. Biochem. Cell Biol. 29 (10) (1997) 1167–1177.
[44] Y. Wang, Y. Lin, H.G. Zhang, J. Zhu, A photodynamic therapy combined with topical 5-aminolevulinic acid and systemic hematoporphyrin derivative is more efficient but less phototoxic for cancer, J. Cancer Res. Clin. Oncol. 142 (4) (2016) 813–821.
[45] V. Lambert, J. Lecomte, S. Hansen, S. Blacher, M.L. Gonzalez, I. Struman, et al., Laser-induced choroidal neovascularization model to study age-related macular degeneration in mice, Nat. Protoc. 8 (11) (2013) 2197–2211.
[46] A. Dubrac, S.E. Kunzel, S.H. Kunzel, J. Li, R.R. Chandran, K. Martin, et al., NCK-dependent pericyte migration promotes pathological neovascularization in ischemic retinopathy, Nat. Commun. 9 (1) (2018) 3463.
[47] E.H.C. van Dijk, S. Fauser, M.B. Breukink, R. Blanco-Garavito, J.M.M. Groenewoud, J.E.E. Keunen, et al., Half-dose photodynamic therapy versus high-density subthreshold micropulse laser treatment in patients with chronic central serous chorioretinopathy: the PLACE trial, Ophthalmol. 125 (10) (2018) 1547–1555.
[48] J. Baek, J.H. Lee, S. Jeon, W.K. Lee, Choroidal morphology and short-term outcomes of combination photodynamic therapy in polypoidal choroidal vasculopathy, Eye 33 (3) (2019) 419–427.
[49] S. Ma, Z. Meng, R. Chen, K.L. Guan, The Hippo pathway: biology and pathophysiology,, Annu. Rev. Biochem. 88 (2019) 577–604.
[50] F. Gibault, M. Corvaisier, F. Bailly, G. Huet, P. Melnyk, P. Cotelle, Non-photoinduced biological properties of verteporfin, Curr. Med. Chem. 23 (11) (2016) 1171–1184.
[51] H. Wei, F. Wang, Y. Wang, T. Li, P. Xiu, J. Zhong, et al., Verteporfin suppresses cell survival, angiogenesis and vasculogenic mimicry of pancreatic ductal adenocarcinoma via disrupting the YAP-TEAD complex, Cancer Sci. 108 (3) (2017) 478–487.
[52] C. Wei, X. Li, The role of photoactivated and non-photoactivated verteporfin on tumor,, Front. Pharmacol. 11 (2020) 557429.
[53] H.J. Choi, H. Zhang, H. Park, K.S. Choi, H.W. Lee, V. Agrawal, et al., Yes-associated protein regulates endothelial cell contact-mediated expression of angiopoietin-2, Nat. Commun. 6 (2015) 6943.
[54] J. He, Q. Bao, Y. Zhang, M. Liu, H. Lv, Y. Liu, et al., Yes-associated protein promotes angiogenesis via signal transducer and activator of transcription 3 in endothelial cells, Circ. Res. 122 (4) (2018) 591–605.
[55] X. Wang, A. Freire Valls, G. Schermann, Y. Shen, I.M. Moya, L. Castro, et al., YAP/TAZ orchestrate VEGF signaling during developmental angiogenesis, Dev. Cell 42 (5) (2017) 462–478, e467.
[56] L.Y. Yu, T.J. Tseng, H.C. Lin, C.L. Hsu, T.X. Lu, C.J. Tsai, et al., Synthetic dysmobility screen unveils an integrated STK40-YAP-MAPK system driving cell migration, Sci. Adv. 7 (31) (2021).
[57] A. Dey, X. Varelas, K.L. Guan, Targeting the Hippo pathway in cancer, fibrosis, wound healing and regenerative medicine, Nat. Rev. Drug Discov. 19 (7) (2020) 480–494.
[58] I.M. Moya, G. Halder, Hippo-YAP/TAZ signalling in organ regeneration and regenerative medicine, Nat. Rev. Mol. Cell Biol. 20 (4) (2019) 211–226.
[59] G.T. Kokame, T.E. deCarlo, K.N. Kaneko, J.N. Omizo, R. Lian, Anti-vascular endothelial growth factor resistance in exudative macular degeneration and polypoidal choroidal vasculopathy, Ophthalmol Retina 3 (9) (2019) 744–752.
[60] M. Suzuki, N. Nagai, K. Izumi-Nagai, H. Shinoda, T. Koto, A. Uchida, et al., Predictive factors for non-response to intravitreal ranibizumab treatment in age-related macular degeneration, Br. J. Ophthalmol. 98 (9) (2014) 1186–1191.
[61] M. Simons, E. Gordon, L. Claesson-Welsh, Mechanisms and regulation of endothelial VEGF receptor signalling, Nat. Rev. Mol. Cell Biol. 17 (10) (2016) 611–625.